

Quantification of Surface Forces of Thermoplastic Elastomeric Nanocomposites Based on Poly(styrene-ethylene-*co*-butylene-styrene) and Clay by Atomic Force Microscopy

Anirban Ganguly, Anil K. Bhowmick

Rubber Technology Center, Indian Institute of Technology, Kharagpur-721 302, India

Received 18 June 2007; accepted 9 August 2008

DOI 10.1002/app.29268

Published online 10 November 2008 in Wiley InterScience (www.interscience.wiley.com).

ABSTRACT: Atomic force microscopy was used for qualitative phase morphological mapping as well as quantitative investigation of surface forces measured at constituting blocks and clay regions of a thermoplastic elastomeric nanocomposite based on triblock copolymer: poly(styrene-ethylene-*co*-butylene-styrene) (SEBS) and organically modified nano-clay. The roughness and power spectral density analyses of surface topography provided the increment in random roughness of the nanocomposite surface compared to pristine SEBS surface. The same surfaces were examined by means of single point force-distance, and force-volume measurements. Large adhesive

force of 25 nN and contact force of 260 nN were found in soft polyethylene (PEB) segments and higher cantilever deflection of 210 nm was found for clay regions of SEBS-clay nanocomposite. Mapping of elastic modulus of the glassy and rubbery blocks and clay regions was probed by employing Hertzian and JKR model from respective approaching and retracting parts of force-distance curves. © 2008 Wiley Periodicals, Inc. *J Appl Polym Sci* 111: 2104–2115, 2009

Key words: force quantification; surface properties; polymer; nanocomposite; AFM; microscopy

INTRODUCTION

Nanotechnology stands as one of the most promising areas of research, among which polymer nanocomposites play a revolutionary role.¹ Polymer layered silicate nanocomposites are the foremost members of such high performance nanocomposites. Although researched for a couple of decades only, first commercially developed polymer nanocomposite was by Toyota group in 1980s.²

New measurement procedures are inevitable in the rapidly burgeoning field of nanotechnology. Information about nanoscale mechanical properties on polymer-nanocomposite surfaces is the present day need in this subject. Among various conventional methods, nanoindentation³ is currently employed for nanoscale mechanical measurements of polymer surfaces. But this process faces serious challenges as dimensions shrink, while too large surface or volume is tested by the large radius of indenter tip and relatively large load is applied. Small diameter of atomic force microscopy (AFM) tip (10–20 nm of tip

radius of curvature), a nonvertical inclined tip trajectory while penetrating the surface, low applied load (in the range of nN only) and intricate scanning capability enable the combination of *in situ* elastic property imaging with nanoscale spatial resolution.

Though transmission electron microscopy and X-ray scattering^{4–10} have been mostly used in the field of polymer nanotechnology, AFM has now proven to be one of the most convenient tools for nonconductive material characterization providing an obvious advantage for polymer surface ever since its inception.¹¹ For surfaces, in addition to nanoscale imaging^{12,13} with spatial resolution nearing as low as 1 nm, AFM provides direct force measurements between its probe and the surface^{14,15} by force-distance (f-d) curves. Nanoscopic force quantification through force between the probe tip and the polymeric phases offers new insights into polymer nanocomposites. These f-d curves not only assess surface interaction forces, but also can predict bulk mechanical properties. This surface force quantification has been mainly emphasized in the field of biological samples^{16–19} without giving enough stress on measurements on polymer surface.

The data in such experiment are acquired in the form of detector voltage versus displacement in z-direction. The detector voltage further can be correlated to the sample surface separation from the

Correspondence to: A. K. Bhowmick (anilkb@rtc.iitkgp.ernet.in).

Contract grant sponsors: DST, AICTE.

probe tip. While in contact, the deflection of the piezo in the *z*-direction is the same as that of the displacement (i.e., deflection) of the cantilever. The force acting on the cantilever by the neat and nanocomposites samples of SEBS can further be calculated by using Hook's law. These AFM force curves are useful to examine the mechanical modulus and viscoelastic properties of polymer samples by relating applied force to the deflection of the cantilever, spring constant, and tip-sample separation.

Apart from force calculation at a single point, 'force volume' imaging for measuring and displaying elasticity at multiple points on the sample surface can be employed where 3-dimensional force measurements are performed as a result of interactions of tip and sample in the entire scan area.

Approximation of AFM probe tip as a spherical one is reasonable in describing forces of interactions by power-law sphere-plane models to describe the probe-sample interactions.²⁰ Hertz model gives the force on a spherical probe (tip is spherical in apex having radius of curvature of 10 nm) as a function of elastic properties of the polymeric domains, the radius of the probe and penetration. It fits the mechanical deformation applied to AFM force curve data.

In our early communication,²¹ we have reported preparation and properties of nanocomposite based on SEBS. The effects of various parameters like surface modification of clay, its dosage, preparation procedures like solution and melt intercalation on the mechanical, dynamic mechanical properties, and morphology have been described. Micro-phase domain morphology of neat SEBS by Motomatsu et al.^{22,23} and nanomechanical investigation of polymer layers by Tsukruk et al.^{24,25} and Nishi et al.^{26–28} have been reported using AFM force measurements.

One of the primary reasons that AFM is a particularly powerful microscopy technique is that digitally stored data can readily be treated mathematically to have quantitative determination of the surface characteristics. Till date, surface force quantification of polymer nanocomposite is a less discussed area of research, though much has been described in the field of biopolymer surfaces by AFM. This article emphasizes 2-dimensional AFM phase morphology, roughness analysis as well as the mapping of 1-dimensional and 3-dimensional surface force and its quantification of poly(styrene-ethylene-*co*-butylene-styrene) (SEBS) and its clay-based nanocomposite by different atomic force measurements. The detailed morphology-property investigation employing AFM tapping and force mode data in this present work is the first of its kind in such styrenic triblock copolymer (SEBS)—organically modified clay based nanocomposites. Earlier, we have characterized a series of nanocomposites based on various rubbers and their nanocomposites^{29–33} by TEM and AFM.³⁴ Map-

ping of AFM phase images of the SEBS-clay nanocomposites has been done by the same authors,²¹ where the effect of nanoclay concentration has been addressed in details and demonstrated that four parts (by weight %) of this organically modified nanoclay (CL) imparts best physico-mechanical properties along with fine dispersion all through the matrix of SEBS. In another publication,³⁵ it has been shown how lamella width changes with impregnation of this CL clay with the aid of AFM. That is why we have taken up this particular clay wt % in this present study.

The present methodology will help in understanding the phase separated morphology and actual forces of interaction on the surface of these block copolymer based nanocomposites.

EXPERIMENTAL SECTION

Materials and method of nanocomposite film preparation

Symmetric triblock copolymer used for the study, poly styrene-(ethylene-*co*-butylene)-styrene having styrene-ethylene butylene-styrene ratio of 15 : 70 : 15 (by weight)^{35,36} and total molecular weight of $M_w = 57,000$ (Kraton G 1652), was generously supplied by Shell Chemical Co. (Washington Blvd., OH, presently Kraton Polymers, Houston, TX). Organically modified montmorillonite nanoclay (CL20) having aliphatic long chain organic modifier, [dimethyl dihydrogenated tallow ($C_{18} : C_{16} : C_{14} = 65\% : 30\% : 5\%$) quaternary ammonium chloride having concentration of 95 mequiv./100 g clay] was procured from Southern Clay Products, Gonzales, TX, USA. Analytical grade toluene and ethanol were obtained from Nice Chemicals Pvt. Ltd. Cochin, India. Finely powdered (4% by weight) modified CL20 clay, dispersed in minimum quantity of ethanol (2% with respect to toluene-SEBS solution) was added to dissolved SEBS (10% solution) in toluene under constant stirring (1000 rpm) at room temperature ($27\text{ }^\circ\text{C} \pm 2\text{ }^\circ\text{C}$) in a Remi stirrer (Mumbai, India). After leaving it in stirring condition for 1 day in dust-free condition, the resultant solution was then allowed to stand for 1 h. Thereafter, the film of nanocomposite was cast on a leveled glass plate and allowed to evaporate the solvent for 2 days at $25\text{ }^\circ\text{C} \pm 2\text{ }^\circ\text{C}$ and 60% relative humidity in a dust free atmosphere. The samples were subsequently dried at $80\text{ }^\circ\text{C}$ till constant weight (for ~ 2 h) to remove any further solvent trace. The thickness of the dry film was 50–60 μm .

Atomic force microscopy

All measurements were performed at ambient condition with a MultiModeTM Nanoscope IIIa AFM

(Digital Instruments/Veeco Metrology Group, Santa Barbara, CA). Small squares ($2 \times 2 \text{ mm}^2$) of SEBS and SEBS-clay nanocomposites were cut from the nanocomposite films and attached to stainless steel sample puck for AFM imaging. Typical scan rate for image acquisition was ~ 1 line/s. For scanning, identical test conditions were maintained in all the measurements. No filtering or other image processing operations were performed to generate the images.

Four types of AFM measurements were carried out for investigating SEBS-clay nanocomposite surface: (a) surface morphological mapping, (b) surface roughness characterization, (c) determination of interaction force at a given point, and (d) force-volume imaging. Although several calibration procedures were established, a nominal spring constant of 0.12 Nm^{-1} of triangular contact mode cantilever was chosen and used for the force measurements³⁷ studies in (c,d). Cantilever was changed to different spring constant of 0.30 Nm^{-1} in a few cases to get a better resolution of force. The force values calculated either from 0.12 Nm^{-1} or 0.30 Nm^{-1} cantilevers give the same number

Surface morphological mapping

Tapping mode AFM images were obtained with etched silicon (model RTE SP, with a spring constant in the range of 40 N/m) probes for morphological investigation. The specified resonance frequency of these tips was $\sim 280 \text{ kHz}$. In this mode, the feedback mechanism was controlled by the set point ratio (defined as $r_{\text{sp}} = A_{\text{sp}}/A_0$) of 0.85 – 0.90 , where A_0 = free oscillation and A_{sp} = set point amplitude in contact with the surface, for the cantilever respectively, selected for the measurement. The scan area was rotated to ensure proper morphology detected by the AFM tip.

Roughness characterization

The changes in surface topography were determined quantitatively by the root mean square (RMS) roughness calculation (R_q). Surface height distribution of the prepared nanocomposite was described by the variation in RMS roughness (R_q) involving the standard deviation of height variations (Z_i) in topographic image

$$R_q = \sqrt{\frac{\sum (Z_i)^2}{n}} \quad (1)$$

Mean roughness, R_a , gave the arithmetic average of the absolute values of the surface height deviations,

Z_j , measured from the mean plane of the surface

$$R_a = \frac{1}{n} \sum_{j=1}^n |Z_j| \quad (2)$$

The R_a and RMS roughness (R_q) analyses gave primary information about the fine-scale variations of the effective surface height. However, when imaged locally, only a fraction of the surface height distribution appeared in the image height distribution.

The power spectral density (PSD) function provided a clearer representation of the surface as it gave the amplitude of the surface roughness as a function of the spatial frequency of features. In this PSD technique, power (roughness amplitude squared) was calculated as a function of spatial wavelengths of the features that contribute to the surface image.^{15,18,33}

$$\text{PSD} = (\text{RMS})^2 \quad (3)$$

The entire image is Fourier decomposed into spatial frequencies utilizing PSD, complete mathematical treatment³⁴ of which is beyond the scope of this article. The PSD describes how the power (or variance) of a time series is distributed with frequency. The spectral density of the wave, when multiplied by an appropriate factor, will give the *power* carried by the wave, per unit frequency. This is then known as the PSD or spectral power distribution (SPD) of the signal. Being power per unit of frequency, the dimensions are those of a power divided by Hz and it can be simply called as the *spectrum* of the signal. In PSD, the smaller features on a surface as high frequency peaks (short wavelengths) appeared on the right hand side of the spectra and the bigger features were placed on the left hand side of the spectra. Because of sinusoidal nature of the composite wave form, relatively smaller set of spectral frequencies describes the entire surface.

Force at a given point

A force sensor of an AFM comprised of a tip (affixed to a cantilever mounted on a base) and a piezo displacement unit, which moved the substrate upward and downward toward the cantilever while the base of the cantilever was kept fixed. At first the topographical/phase images were checked for particular domains and then force-distance measurement was done exactly on the particular small area by point-shoot force measurement available with the software.

As the substrate interacted with the probe, the cantilever was deflected from its normal horizontal position and subsequently the tip jumped into

contact (snap-in) with the substrate surface. The piezo unit continued its upward movement until a preset z -coordinate value was achieved. Then, the cantilever reversed its direction of movement. As soon as the restoring force F of the cantilever became equal to the interaction force of the cantilever, the tip was separated from the surface of the substrate. By means of the reflection angle of a laser beam reflected at the surface of the cantilever, the extent of the cantilever deflection was measured. On interacting with sample surface, the force experienced by the cantilever (F) was measured from a plot of the cantilever deflection, as a function of sample position, x , at the moment of separation along the z -axis (i.e., towards or away from the probe tip) or z -piezo translation and its spring constant, (k) by using Hook's law,

$$F = -k.x \quad (4)$$

These AFM force curves so acquired from cantilever deflection and stiffness were useful to examine the mechanical modulus and viscoelastic properties of SEBS-clay nanocomposite film surfaces in the present investigation. Equation (4) describes force as a function of z -piezo movement i.e., penetration travel in Z -direction. But for usefulness, these force curves were transformed into force as a function of distance, d , between the sample and the tip. The horizontal distance axis (nm) was converted from Z -piezo movements to probe-sample surface separation by subtracting the cantilever deflection amplitude (nm) from the Z -piezo displacement for each data set in each force curve. Force-displacement of piezo curves were transformed into corrected force-distance curve.

Force volume imaging

To obtain spatial distribution of multiple force-distance data, force-volume (FV) measurements³⁶ for selected surface areas were carried out with a scan rate of 1 Hz using a relative trigger mode. A force-volume scan consists of a series of force determined at various points on the surface.

The acquisition time for a single force curve was 0.1 s. The topography of the surface was scanned and set point value was set before the adhesion map at multiple points. A force-volume window consisted of three different types of informations: the height image, the FV image, and deflection curves at each selected points. In FV, force curves were obtained while the AFM tip scanned the surface to have a two dimensional array of force-distance curves over the entire scanned surface. For determining relative elasticity of localized regions, amplitude of tip deflection versus sample position was recorded.

RESULTS AND DISCUSSION

Examination of surface phase morphology

Phase images in Figure 1(a,b) reveals the morphology of pristine SEBS and its clay based nanocomposites scanned in tapping mode of AFM. In the well-ordered phase-separated morphology, constituting domains arranged in worm-like lamellar fashion in dark-bright contrast can be observed. In the dark-bright contrast [Fig. 1(a,b)], bright cylindrical domains correspond to hard styrenic phases, while the darker domains are due to softer ethylene-*co*-butylene phases of SEBS. Basically, this phase contrast in tapping mode is due to difference in energy dissipation between the probe tip and the viscoelastic SEBS-clay sample surface during the tapping cycles. Since the tapping amplitude is kept constant, the energy dissipation mainly depends on the mechanical properties^{12,13} of the aforesaid sample. The origin of this lamellar structure of PS component is due to its higher surface energy (40 mJ m^{-2}) than that of PEB component ($\sim 23 \text{ mJ m}^{-2}$).³⁵ The alternate distribution of low and high modulus (brighter domains) regions in the nanocomposites with occasional occurrence of most bright (highest modulus) clay regions is evident from the phase image in Figure 1(b).

The stronger penetration of AFM tip in the softer PEB region relative to hard PS region (elastic moduli of these two components are expected to differ in magnitude) makes visualization of different phase-components as shown in Figure 1(a). The contrast in phase images is related to difference in stiffness of the constituting blocks, spring constant, and cantilever damping from tip-sample interactions.¹² Only four parts by weight of the organically modified montmorillonite clay is responsible for the evolution of a widened nano-phase separated morphology [Fig. 1(a,b)], where the clay plates of dimension 40–54 nm in length and 4–17 nm in width, are embedded in the soft rubbery phases in the block copolymeric matrix as shown (with arrow marks) in Figure 1(b). Because of tip-broadening effect by AFM tip (of nominal tip radius of curvature $\sim 20 \text{ nm}$), the gap between adjacent clay layers does come out to be very clear in Figure 1(b). These are not defects or agglomerated clay layers. These are intercalated clay with occasional exfoliated layers (checked and proved by X-ray diffraction and transmission electron studies also, presented elsewhere). In the new morphology, the soft phases are widened to 50–75 nm patches from their original width of 12–15 nm, where nanoclays are embedded in the matrix.

Roughness and power spectral analysis

The smoothness of the neat SEBS and its clay based nanocomposite surfaces has been characterized by

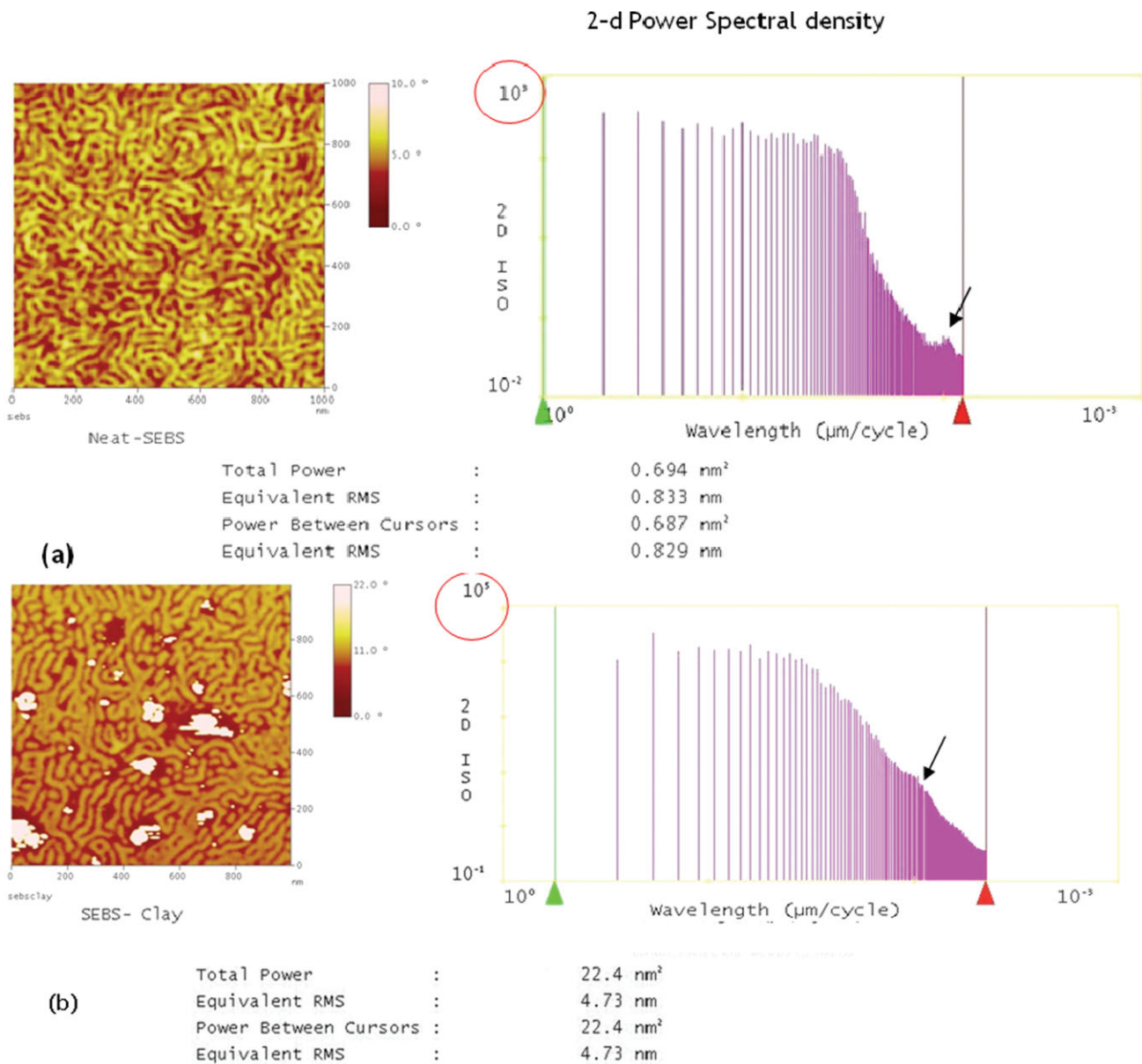


Figure 1 Intermittent mode phase image of (a) neat SEBS and (b) SEBS-clay nanocomposite along with their respective power spectral density plots and calculations. [Color figure can be viewed in the online issue, which is available at www.interscience.wiley.com.]

RMS roughness and PSD (Fig. 1) analysis. The height deviations as well as the lateral spacing of the surface features are performed by PSD. This PSD function reveals distribution of periodic surface features [Fig. 1(a,b)]. PSD depends upon squaring the fast Fourier transform of the image and hence for a range of spatial frequencies, the total power³⁴ of the surface equals the RMS roughness squared³⁶ as per eq. (3).

The values of RMS, total power, and equivalent RMS (root-mean-square roughness of the sample contributed by the frequencies and calculated as the square root of the integral of the power) are reported in Table I. The RMS roughness of the neat

SEBS surface is found to be within 1 nm range and its corresponding power spectral analysis also gives a low equivalent RMS (<1 nm).

TABLE I
Surface Roughness Quantification for Neat and Nanoclay Based Nanocomposites of SEBS

Parameters	Neat SEBS	SEBS-clay nanocomposite
RMS (R_q), nm	0.81	4.62
R_a (nm)	0.65	1.85
Equiv. RMS ^a (R_q), nm	0.83	4.73
Total power ^a , nm ²	0.69	22.4

^a Calculated from the power spectral density measurements of images in Figure 1 (a–b).

The RMS roughness increases effectively to 4.6 nm for the clay-based SEBS nanocomposite, as shown in Table I. The difference between average roughness and root mean square roughness, ($R_a - R_q$), is increased from neat SEBS to its clay-based nanocomposite (Table I), indicating the presence of randomness in surface after clay incorporation. Still, the surface remains well within the limit for carrying out the force measurements by AFM probe.

The PSD is useful in analyzing surface roughness. This PSD is a representation of amplitude of a surface roughness as a function of spatial frequency (inverse of spatial wavelength) of roughness features. Power spectrum is a plot of power as a function of spatial wavelength or frequency. Total power is RMS roughness amplitude squared (RAS).

Following the RMS (R_q) and R_a roughness measurements (Table I), two-dimensional power spectral density (2-D PSD) calculation was performed on the images and plotted against each other (neat and nanocomposite images) as shown in Figure 1(a,b). In this 2-D PSD, power (y -axis, nm^2 units) is plotted against spatial wavelength (x -axis, $\mu\text{m}/\text{cycle}$ units). Fractal nature of neat SEBS and its clay based nanocomposite is evident from the plateau in the power versus spatial wavelength plot in PSD [Fig. 1(a,b) respectively]. More than 30-fold increase in total power as a result of impregnated nanoclays is observed in the PSD of the nanocomposite as compared to the neat SEBS one (Table I). At the same time, the equivalent RMS obtained from PSD calculations also increases significantly to sixfold for 2-dimensional PSD of the nanocomposite. This value has well agreement with the increment in RMS roughness within the same pair of surfaces (Table I). Shift in the higher frequency features in the PSD plot of SEBS-clay nanocomposite indicates an increase in domain width as indicated by arrow marks in Figure 1(a,b). For better understanding, the vertical roughness of the respective surfaces of neat SEBS and its clay based nanocomposite is provided in Figure 2.

'Force' determined at a given point

When AFM tip makes single indentation or a single penetration into SEBS sample, the information is collected about the displacement of the cantilever. As a result of this experiment a force-distance curve is obtained. The original force-distance curve is provided in Figure 3 for neat SEBS. More specifically, the scan is carried out on PS part of SEBS-clay only. Force curves are generated when AFM probe tip approaches and interacts with the SEBS-clay nanocomposite surface. An entire force curve comprises of approaching and retracting [$a-b-c'$ and $d-e-f-a'$ respectively, in Fig. 3(a,b)] traces. Dissection of a typical force plot ($a-b-c-d-e-f-a'$) for SEBS-clay nano-

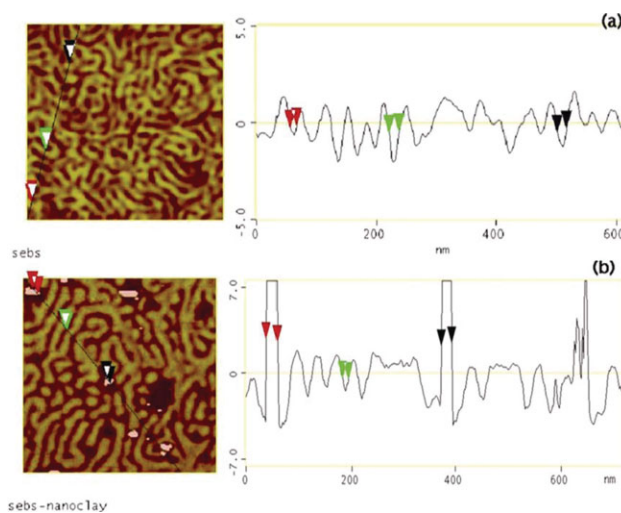


Figure 2 Roughness measurement of (a) neat SEBS and (b) SEBS-clay surfaces. [Color figure can be viewed in the online issue, which is available at www.interscience.wiley.com.]

composite-tip interaction is illustrated in Figure 3(b,c). Probe's deflection is plotted in vertical axis while horizontal axis plots the probe's movement (in actual piezo extension or retraction) relative to the sample. Force-displacement of piezo curve for PS region of the SEBS-clay nanocomposite [Fig. 3(b)] has been transformed into corrected force-separation plot for the same region in Figure 3(c).

At first, during the approaching process, the hard tip surface (made of Si_3N_4) approaches SEBS-clay nanocomposite surface without any long-range attraction as indicated by the flat plateau portion of the curve [a' in Fig. 3(a,b)] which does not show any deflection of the cantilever. When the tip comes within the proximity of a few nanometer from the sample surface, the attractive force gradient of the tip and the sample causes the downward deflection of tip to snap-in or jump-to contact [b' in Fig. 3(a,b)] to the surface due to the attractive force gradient exceeding the spring constant, k . As the tip presses into the surface, the cantilever bends upward [c' in Fig. 3(a,b)].

As the piezo retracts in the z -direction, the upward force gradually cancels the surface attraction (the flat zero-deflection line indicates zero externally applied load). The tip momentarily passes through the original 0 deflection point [d' in Fig. 3(a,b)] and ultimately goes into the repulsive regime. While retracting, the force curve follows the approach curve up to the set point value and then shows hysteresis ($b-c-d-e-f-a'$) below the zero deflection line. Because of difference in viscoelastic nature of sample domains in this SEBS-clay nanocomposite, the aforesaid adhesion hysteresis loop area and pull-off forces vary from domain to domain (Table II).

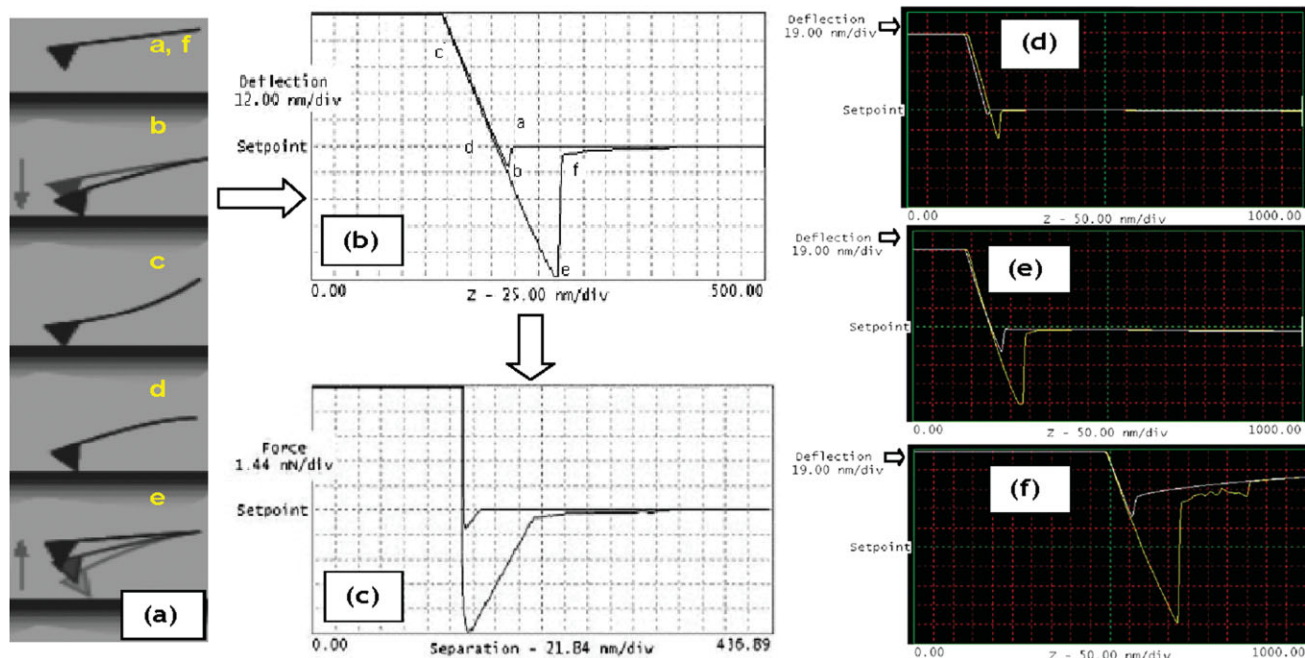


Figure 3 (a) Steps in AFM force measurements on a single point. (b) Force plot: cantilever deflection versus deflection of piezo in z-direction and (c) corrected force-distance curve: tip-sample force versus tip-sample separation for a SEBS nanocomposite. Individual force distance curves on (d) clay, (e) hard styrenic and (f) soft rubbery block of SEBS-clay nanocomposite. [Color figure can be viewed in the online issue, which is available at www.interscience.wiley.com.]

Finally, the tip breaks free off the surface attraction [*e-f* in Fig. 3(a,b)]. The probe rebounds sharply upwards to give force relaxation from which ‘pull-off’ force is determined—characteristics of soft or hard blocks or clay particles of the examined nanocomposite surface. The horizontal distance between *e* and *f* gives the measure of how much the tip traverses in the attractive regime. The tip continues its ascent and becomes free in air again (*f* or *a*).

Because the contact mode AFM tip spring is sufficiently compliant (low stiffness of 0.12 Nm^{-1}), the pull-off force corresponds to the attractive force. And for the same reason the use of tapping mode tips are avoided in calculating all these critical forces.³⁶ The snap-in force and pull-off deflections are not measured with much clarity with tapping mode tips for the higher spring constant value

(ranging from 20 to 80 Nm^{-1} compared to less than 1 Nm^{-1} for contact mode probe) with respect to polymer surface modulus. Typical contact areas are in the order of a few nm^2 during pull-off in case of SEBS as shown in Figure 4.

Pull off force corresponding to the attractive force (Table II) is found to be maximum (25 nN) for softer mid blocks as compared with the harder end blocks (15 nN) or hard clay regions ($\sim 2 \text{ nN}$), as shown in Figure 5. The contact force determined from the horizontal contact portion of the force-distance curve (\odot in Fig. 4), is maximum for mid blocks (PEB), minimum for clay regions and the values for PS domains lie in-between (Fig. 5 and Table II). The ‘jump-to-contact’ (snap-in) depth force also shows a maximum value for the same mid rubbery blocks. The clay regions, being hardest part of the nanocomposite

TABLE II
Force Calculation from Force-Distance Curves for SEBS-Clay Nanocomposite

Matrices/Properties	SEBS-clay nanocomposite		
	PEB block	PS block	Clay
Adhesive force (nN) ^a	25 ± 3	15 ± 2	2 ± 0.5
Contact force (nN) ^b	260 ± 6.1	203 ± 3.6	15 ± 2
Snap-in (nN) ^c	6 ± 0.5	3.3 ± 0.5	0.2
Snap-in depth (Z direction, nm)	30 ± 1.5	18 ± 1	0.5 ± 0.1
Tip-deflection (nm)	107 ± 2.6	188 ± 3	210 ± 3.0

^a Calculated from ‘pull-off’ in the corrected force-distance curves.

^b Calculated from horizontal portion of force plots.

^c Calculated from ‘jump to contact’, in the force plots.

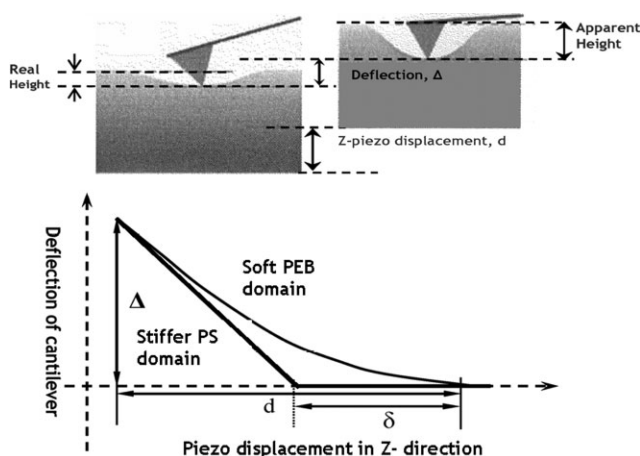


Figure 4 Procedure of force mapping from the f-d curves during interaction and schematic of deflection and penetration in f-d curves

system, deflect the cantilever to the maximum extent of 210 nm as compared with a value of 107 nm for soft blocks. From similar calculations, hard clay regions are found to be most repulsive and least adhering in nature from snap-in force and depth calculations (Fig. 5 and Table II). This information on SEBS-clay nanocomposite system has not been reported before.

‘Force volume’ imaging

The basic approach to examine the spatial distribution of the forces within that volume using an AFM is to collect an array of two-dimensional force-distance curves (Fig. 6). The up and down movement of the sample surface (with respect to tip) allows the building of map of adhesion image or ‘force topography’ image. But the acquired ‘force topography’ image [Fig. 6(a)] is not as sharp as conventional AFM morphological image [Fig. 1(a,b)]. Instead it resembles mosaic of force data collections. ‘Real height image’ can be reconstructed for such rubber-clay nanocomposite if a curve fitting technique is employed for the obtained force-distance curves. As force topography is constructed by multiple point force calculations, it does not always perfectly match with the resolution of contact mode or tapping mode height images. The limitation of total number of data for any given force-volume image file to be restricted³⁷ within a maximum of 1 megabyte (mb) by the relation:

$$(\text{Force per line})^2 \times \text{number of sample} \times 4 \leq 1 \text{ mb} \tag{5}$$

This poses a restriction to a higher resolution in the existing software to the force curves and force

volume images as given in eq. (5). In force-volume images acquired, the effect of data points on force topography has also been shown. In the representative force volume image [with 64 × 64 data points in Fig. 6(a)], the effect of lower data points has diminished the sharpness of the force topography and force plots. On increasing the data points to 256 × 256, the force topographical image as well as force curve contrast has been increased as shown in Figure 6(b) for the same scan area of 2 × 2 μm².

As a result, an array of force curves is stored in the x-, y-, and z-coordinates of each point of a substrate surface range. These FV images allow the investigation of spatial distribution of adhesion forces between probe and sample over the given surface area. The FV force plots contain an array of force curves and the FV imaging contains an array of Z-piezo positions at the points of deflections of force curves. These images provide a 3-dimensional, laterally resolved description of the SEBS-clay nanocomposite surface. In the relative trigger mode, the deflection with respect to undeflected cantilever is used as beginning of curve. This relative trigger mode compensates for the cantilever drift during the scanning to avoid any possible damage of either probe or the surface. X, Y and Z are three selected points on the entire image, where clay, hard polystyrene, and soft poly ethylene butylene zones respectively, have been recognized in the height image prior to force calculation. Three arrays of forces are charted in Table II. The corresponding force-volume image [Fig. 6(a,b)] shows gradual increment of tracking force from clay region to soft polyethylene butylene regions.

It may be mentioned here that the slope of the plot (sensitivity) comes into play for the calculation of force. The sensitivity factor varies from clay region (~ 1) to PS region (~ 7) to PEB region (~ 10).

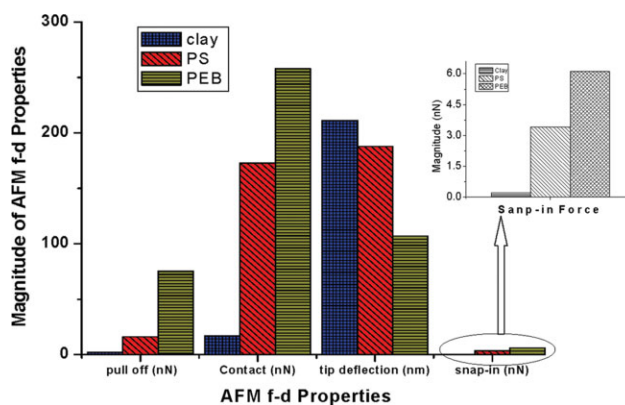


Figure 5 Forces of interactions on blocks and nanoclay of SEBS-clay nanocomposite taken from force volume experiments (snap-in forces in constituting blocks shown in the inset). [Color figure can be viewed in the online issue, which is available at www.interscience.wiley.com.]

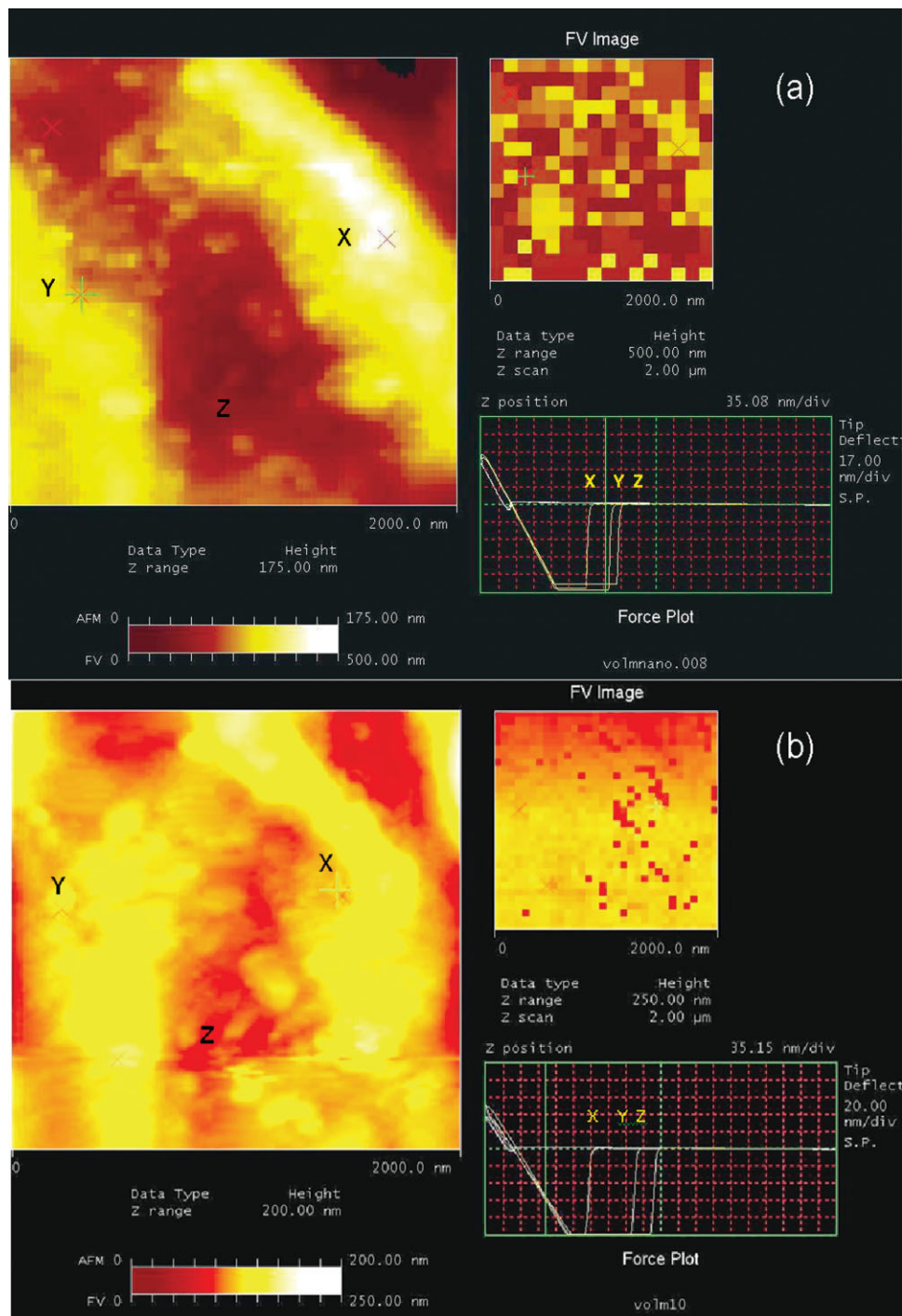


Figure 6 Force volume imaging with force topography calculated taking (a) less (64×64), (b) more (256×256) data points on the SEBS-clay nanocomposite surface. [Color figure can be viewed in the online issue, which is available at www.interscience.wiley.com.]

This sensitivity factor is multiplied with the displacement \times stiffness term to get actual force.

Elasticity maps

Nano-mechanical data are extracted from analysis of AFM force-distance curve of SEBS-clay nanocomposites. Among variety of theoretical models describing

mechanical contact between two bodies under external load in analyzing force-distance curves, Hertz theory^{38,39} has been most widely used where the absence of adhesion is assumed. JKR theory⁴⁰ is adopted to treat adhesive interactions. Hertz mechanics is used for simplicity where AFM probe tip has hemispherical shape. It makes the discussion easier and tangible to readers focused in the

TABLE III
Modulus of SEBS-Clay Nanocomposites from Models and its Actual Bulk Modulus

Block and clay regions of SEBS nanocomposite	Modulus from Hertz Model, (E_{Sample}), MPa	Localized sample deformation, (δ), nm	Modulus from JKR Model, ($E_{\text{Sample}}^{\text{JKR}}$), MPa	Bulk modulus ^a of SEBS-clay nanocomposite, MPa
Soft PEB block	12 ± 1	50	15 ± 1	26 ± 1
Hard PS block	22 ± 1	30	24 ± 1	
Clay regions	100 ± 5	2	105 ± 5	

^a Measured with 50 mm/min strain rate in Universal Testing Machine Zwick 1445, Ulm, Germany.

approaching f-d curve. When the cantilever approaches stiff sample surface, deflection of cantilever, Δ , becomes equal to Z-piezo displacement, d (Fig. 4), whereas this 'd' becomes larger to attain *pre-set* trigger value of cantilever deflection in the case of rubber sample due to deformation of the sample itself (δ).⁴¹

As the rubber samples undergo quick relaxation on applying nano-Newton levels of load by AFM tip, it has been observed from the phenomenon of the delay ramp in the force-curves after giving 10 s of delay. Then the applicability of the Hertzian contact mechanics^{38,39} to the force curve is hence justified. On releasing the load, AFM tip leaves almost no mark of indentation of the rubbery SEBS-clay surface (not shown in the picture).

To determine the elastic properties of SEBS-clay nanocomposites in its different constituting zones, the corrected force-distance curve has been fitted to the Hertz model,

$$\delta = \sqrt{\frac{\pi \cdot k \cdot \Delta \cdot (1 - \nu^2)}{2 \cdot E \tan \alpha}} \quad (6)$$

where δ , depth of penetration on the domains as shown in schematic presentation in Figure 4, and E , the stiffness from load curve (the contact portion of force curves). α is the half angle of the tip geometry. $k \cdot \Delta$ gives the force exerted on SEBS sample. The penetration by the tip, δ is measured from difference between cantilever traversed, i.e., the difference between (distance traversed from just contact point to present z scan position calculated from force plot) and (the difference between non contact deflection and present deflection at present z position) is given directly by *Nanoscope* software attached with AFM instrument. Modulus of the sample (E_{sample}) can be calculated from δ ,^{41,42} using eq. (7),

$$\delta = 0.825 \left[\frac{k^2 (R_{\text{tip}} + w_{\text{sample}}) \cdot (1 - \nu_{\text{sample}}^2)^{2/3}}{E_{\text{sample}}^2 \cdot R_{\text{tip}} \cdot w_{\text{sample}}} \right]^{1/3} \cdot (d^*)^{2/3} \quad (7)$$

and assuming the AFM tip apex as sphere and the AFM cantilever as a spring attached to the sphere in series. k is the spring constant (0.12 Nm⁻¹) for con-

tact mode AFM tip, R_{tip} is the radius of curvature of the hemi-spherical portion of the apex of the contact mode tip, ~ 10 nm, w_{sample} is assumed to be the lamellar width or thickness of the domains or the clay regions on the surface of nanocomposite under investigation. ν_{sample} is the Poisson's ratio^{42,43} of the selected segments on the surface, namely soft PEB (0.5), harder PS (0.33) and clay (0.25).

In an ambient condition, in air, the primary source of this adhesion is the formation of a capillary bridge between the tip and the surface. Then pulling the tip out of that bridge requires a measurable force (in the range of nN) to get rid of the surface tension.

Tip-sample contact points have been correctly determined by the *Nanoscope* software. The work done by the cantilever is related to local mechanical properties. Slope gradient which is obtained from the approaching f-d curve (i.e., the contact part) is directly related to surface stiffness. This contact part of the f-d curves for various portions of SEBS-clay nanocomposite sample is used to map the elasticity of the sample domains quantitatively. On the hardest clay regions the slope is unity, while on PS domains of SEBS nanocomposite, the slope becomes near to but less than unity. On more compliant domain, i.e., the softer PEB lamellae, the probe tip penetrates more than in the case of hard PS domains. As a result, the slope in the later case is less than that of the clay and PS regions.

The harder the domain, the more is the deflection of the penetrating probe tip (the Z scale). The highest tip-deflection is observed for the clay particles whereas it is minimum in the case of soft PEB region quantifying the former to be most stiff region in the said nanocomposite. The force plot indicates almost no or very less attractive nature of the clay region as shown by almost zero snap-in and less pull-off force. Maximum tip snap-in, pull-off, and contact force indicate the most adhesive nature of the soft PEB blocks in the nanocomposites.

Thus E_{sample} has been calculated for constituting domains of the nanocomposites -PS and PEB and nanoclays regions in the SEBS-clay nanocomposite from eq. (7) and is provided in Table III, where modulus of the clay platelets is found to be 102 MPa, while the modulus for PS and PEB blocks are

determined to be 22 and 12 MPa, respectively. These modulus values are comparable with the slow strain-rate macro mechanical tensile data of 26 MPa for SEBS-clay nanocomposite (shown in Table III). The lower calculated modulus values of nanoclays compared to the literature may be due to adhering soft rubber on the nanoclays which reduces the overall modulus of clay regions in the composite.

Because of adhesive interaction in retracting portion of the *f*-*d* curve, JKR model⁴⁰ registers better insight into nano-mechanical measurements of forces, where large deformation and adhesive energy is involved. Elastic modulus of the sample can be obtained from JKR theory by

$$E_{\text{Sample}}^{\text{JKR}} \approx 0.95 * \frac{F_{\text{adh}}(1 - \nu^2)}{\sqrt{R * \delta^3}} \quad (8)$$

where F_{adh} is the pull-off force, ν is the poisson's ratio, R is the radius of curvature of the probe tip, and δ is the localized sample deformation in PS or PEB or clay regions in SEBS-clay nanocomposite (Fig. 4).

From the calculation in eq. (8), the softer PEB region is shown to have maximum adhesive force in nature (Fig. 6 and Table II) with the calculated modulus in the range of 15 ± 1 MPa (Table III). The harder PS domains found to have modulus in the range of 24 ± 1 MPa in the SEBS-clay nanocomposite. As in the processed nanocomposites, clays might have coated with thin SEBS layers, thus the observed values for clay modulus ranges in the region of ~ 100 MPa which is much less than that of the literature values for clays in the GPa range. The discussion infers that the bulk modulus of the SEBS clay nanocomposite (26 ± 1 MPa as shown in Table III) is dictated by the contribution from hard PS nano-domains and clay layers in the matrix.

CONCLUSIONS

1. AFM was successfully used for surface characterization of solution cast poly(styrene-ethylene-*co*-butylene)-organically modified clay nanocomposites by topographic and phase images.
2. The surface phase morphological images clearly exhibited a well ordered nano-phase separated lamellar morphology in dark-bright phase contrast for neat SEBS and its organically modified nanoclay impregnated nanocomposites. The bright domains corresponded to hard polystyrene lamella and the darker domains to softer rubbery ethylene-*co*-butylene lamellae.
3. Four parts of organically modified nanoclay, when impregnated on the surface, widened the softer PEB lamella width from original 12–15 nm to patchy domains of dimension 50–75 nm in the corresponding nanocomposites creating

rubbery patches from the clay-impregnated regions. The typical width of most bright clay platelets was observed in the range of 4–17 nm.

4. Impregnation of organically modified nanoclay essentially increased the mean and RMS roughness of the resulted surface. The roughness and power spectral analysis of surface topography of the corresponding nanocomposite surface provided smoothness in the range of 0.5–2.5 nm. Fractal nature of neat SEBS and its clay based nanocomposite was evident from the plateau in the spatial wavelength versus power plot where a more than 30-fold increase in total power and sixfold in equivalent RMS 2-dimensional PSD resulted in the nanocomposite as compared to the neat SEBS one. The increase in domain width was observed from the shift in the higher frequency features in the PSD plot.
5. Qualitative and quantitative investigation of surface forces of interaction for the neat SEBS and its nanocomposite measured at constituting blocks and clay regions by force-distance plots was done on single points and on entire force volume. Maximum adhesive force of 25 nN was found in rubbery PEB segments and cantilever deflection was found to be maximum (210 nm) for clay regions both in single point force mapping and entire force volume force mapping of SEBS-clay nanocomposite under investigation.
6. The calculated modulus of the soft and the hard blocks from AFM force-distance analysis were 16 and 24 MPa respectively, tallied with the slow strain-rate macro mechanical tensile strength of 26 MPa for SEBS-clay nanocomposite, while that for clay regions was found to be about 100 MPa employing Hertz and JKR models to force-distance curves.

The authors thank Thomas Mueller and Dr. Bede Pittinger of Veeco Metrology Group, CA, USA, for their helpful suggestions in AFM experimentations.

References

1. Krishnamoorti, R.; Vaia, R. A. *Polymer Nanocomposites: Synthesis, Characterization, and Modeling*; ACS: Washington, DC, Symposium Series 804, 2001.
2. Usuki, A.; Kojima, Y.; Kawasumi, M.; Fukushima, Y.; Okada, A.; Kurauchi, T.; Kamigaito, O. *J Mater Res* 1993, 8, 1775.
3. Oliver, W. C.; Pharr, G. C. *J Mater Res* 1992, 7, 1564.
4. Sawyer, L. C.; Grubb, D. T. *Polymer Microscopy*; Chapman & Hall: New York, USA, 1987.
5. Meier, H.; Strobl, G. R. *Macromolecules* 1987, 20, 649.
6. Han, C. D.; Kim, J.; Kim, J. K. *Macromolecules* 1989, 22, 383.
7. Leung, O. M.; Cynthia, G. M. *Sci Rep* 1992, 55, 64.
8. Sakurai, S.; Kawada, H.; Hashimoto, T. *Macromolecules* 1993, 26, 5796.

9. Heck, B.; Arends, P.; Ganter, M.; Kressler, J.; Stuhn, B. *Macromolecules* 1997, 30, 4559.
10. Morgan, A. B.; Gilman, J. W. *J Appl Polym Sci* 2003, 87, 1329.
11. Bining, G.; Quate, G. C. F.; Gerber, C. *Phys Rev Lett* 1986, 56, 930.
12. Magonov, S. N.; Ellings, V.; Whangbo, M. H. *Surf Sci* 1997, 375, L385.
13. Bar, G.; Thoman, Y.; Whangbo, M.-H. *Langmuir* 1998, 14, 1219.
14. Radmacher, M.; Tillmann, R. W.; Gaub, H. E. *Biophys J* 1993, 64, 735.
15. Skolnik, A. M.; Hughes, W. C.; Augustine, B. H. *Chem Educ* 2000, 5, 8.
16. Laney, D. E.; Garcia, R. A.; Parson, S. M.; Hansma, H. G. *Biophys J* 1997, 72, 806.
17. Fang, H. H. P.; Chan, K.-Y.; Xu, L.-C. *J Microbiol Methods* 2000, 4, 89.
18. Smith, J. R.; Swift, J. A. *J Microsc* 2002, 206, 182 and references therein.
19. Gad, M.; Toh, I.; Ikai, A. *Cell Biol Inter* 1997, 21, 697.
20. Israelachvili, J. N. *Intermolecular and Surface Forces with Applications to Colloidal and Biological Systems*, 2nd ed.; Academic Press/Elsevier: New York, 1992.
21. Ganguly, A.; Desarkar, M.; Bhowmick, A. K. *J Appl Polym Sci* 2006, 100, 2040.
22. Motomatsu, M.; Mizutani, W.; Tokumoto, H. *Polymer* 1997, 38, 1779.
23. Luzinov, I.; Julthongpiput, D.; Tsukruk, V. V. *Polym Commun* 2001, 42, 2267.
24. Tsukruk, V. V.; Sidorenko, A.; Gorbunov, V. V.; Chizhik, S. A. *Langmuir* 2001, 17, 6715.
25. Tsukruk, V. V.; Huang, Z.; Chizhik, S. A.; Gorbunov, V. V. *J Mater Sci* 1998, 33, 4905.
26. Nishi, T.; Nukaga, H.; Fujiyami, S.; Nakajima, K. *Chin J Polym Sci* 2007, 25, 35.
27. Watabe, H.; Komura, M.; Nakajima, K.; Nishi, T. *Jap J Appl Phys* 2005, 44, 5393.
28. Komura, M.; Qiu, Z.; Ikehara, T.; Nakajima, K.; Nishi, T. *Polym J* 2006, 38, 31.
29. Sadhu, S.; Bhowmick, A. K. *Rubber Chem Technol* 2003, 76, 860.
30. Sadhu, S.; Bhowmick, A. K. *J Polym Sci Part B: Polym Phys* 2004, 42, 1573.
31. Maiti, M.; Sadhu, S.; Bhowmick, A. K. *J Polym Sci Part B: Polym Phys* 2004, 42, 4489.
32. Sadhu, S.; Bhowmick, A. K. *J Mater Sci* 2005, 41, 1633.
33. Bandyopadhyay, A.; DeSarkar, M.; Bhowmick, A. K. *J Mater Sci* 2006, 41, 5981.
34. Maiti, M.; Bhowmick, A. K. *Polymer* 2006, 47, 6156.
35. Ganguly, A.; Desarkar, M.; Bhowmick, A. K. *J Polym Sci Part B: Polym Phys* 2007, 45, 52.
36. Fang, S. J.; Haplepete, S.; Chen, W.; Helms, C. R.; Edwards, H. *J Appl Phys* 1997, 82, 5891.
37. Digital Instruments. *MultiMode™ SPM Instruction Manual Version 4.31ce*; Digital Instruments: Santa Barbara, CA, 2002.
38. Hertz, H. *J Angew Math* 1882, 92, 156.
39. Garcia, R.; Perez, R. *Surf Sci Rep* 2002, 47, 197.
40. Sun, Y.; Akhremitchev, B.; Walker, G. C. *Polym Mater: Sci Eng* 2003, 88, 417.
41. Skulason, H.; Frisbie, C. D. *Anal Chem* 2002, 74, 3096.
42. Mao, G.; Liang, X.; Simon, K. Y. N. *Encyclopedia of Nanoscience and Nanotechnology*; Marcel Dekker Inc.: New York, 2004; p 933.
43. Weurker, R. G. *Annotated Tables of Strength & Elastic Properties of Rocks*; Drilling Reprint Series, S. P. E.: Dallas, TX, 1963.